Journal of Information Systems Engineering and Management
2025, 10(1)
e-ISSN: 2468-4376
https://www.jisem-journal.com/

Research Article

Bending Analysis of Linear and Non-Linear Functionally Graded Carbon Nanotube Reinforced Nanocomposite Plates with Temperature-Dependent Material Properties

Amirat Hamza*[1], Chiker Yasser[1], Bachene Mourad[1], Guemana Mouloud[2], Iskander Yahia[3]
[1]*Laboratory of Mechanics, Physics, Mathematical Modeling (LMP2M), University of Medea, Medea, Algeria*
[2]*Laboratory of Applied Automation and Industrial Diagnostic (LAADI), University of Djelfa, Algeria*
[3]*Civil Engineering Department, College of Engineering and Architecture, Umm Al Qura University*

Corresponding Author:E-mail: amirat.hamza@univ-medea.dz*

ARTICLE INFO

Received: 12 Jul 2024
Revised: 10 Nov 2024
Accepted: 23 Mar 2025
Published: 25-May-2025

ABSTRACT

This article offers an extensive examination of the bending characteristics of functionally graded carbon nanotube-reinforced composite (CNT-RC) plates with material properties that depend on temperature. It investigates both uniform and non-uniform (functionally graded) arrangements of CNTs throughout the thickness of the plate, addressing an existing research gap. The effective material characteristics of the CNT-RC plates, taking into account the influences of temperature and moisture, are calculated using the extended rule of mixtures. The study employs first-order shear deformation theory (FSDT) to establish the governing equations, integrating thermo-elastic relationships, which are numerically addressed through the finite element method. A validation study verifies the precision of the proposed methodology. A detailed parametric analysis is performed to assess the effects of crucial elements such as plate geometry (length-to-width and width-to-thickness ratios), CNT volume fraction, boundary conditions, and both linear and non-linear CNT distribution schemes on the bending behavior of the CNT-RC plates. This research provides significant insights into the design and optimization of CNT-reinforced composite materials for advanced engineering uses.

Keywords: Bending analysis,temperature-dependent material properties, functionally graded, carbon nanotube-reinforced composite, first-order shear deformation theory, finite element method.

1. INTRODUCTION

The creation of carbon nanotubes (CNTs) by Iijima in 1991 represented a groundbreaking advancement in materials science, owing to their outstanding mechanical, thermal, and electrical properties. These nanomaterials are lauded for their high tensile strength, low density, and superior thermal and electrical conductivity, making them essential in the development of advanced composite materials. The addition of CNTs into polymer and metal matrices has significantly elevated stiffness, strength, and thermal stability, enabling their application in aerospace, automotive, and structural engineering. Functionally Graded Carbon Nanotube Reinforced Composites (FG-CNTRCs) have emerged as a distinct class of functionally graded materials (FGMs), defined by compositions that change spatially to boost performance. FG-CNTRCs employ non-uniform CNT placements to achieve tailored mechanical responses, such as improved bending strength and vibrational resilience. These advanced composites possess substantial potential in designing lightweight yet strong structures for challenging thermal and mechanical conditions.

The distribution pattern of CNTs is one of the most crucial factors affecting the mechanical properties of FG-CNTRC plates. Shen (2009) was the pioneer in exploring nonlinear bending in thermal settings, introducing the concept of functionally graded CNT distributions. Chiker et al. (2020) demonstrated that nonlinear distribution types, such as X-type, significantly enhance vibrational stability and bending stiffness. Similarly, Lazar et al. (2023) emphasized the significance of exponential CNT distribution laws in achieving improved vibrational frequencies, exceeding those of linear and power-law configurations. Mao and Zhang (2018) studied the linear and nonlinear vibration behaviors of graphene-reinforced plates, highlighting the mechanical advantages of tailored CNT distributions. Maoudj et al. (2023) extended this research to cracked FG-CNTRC plates, showing that X-type distributions provide greater resistance to vibrational degradation.The incorporation of CNTs into polymer composites also enhances thermal conductivities. Studies by Jiang et al. (2009) and Zhu, Pan, and Roy (2007) established a foundation for understanding the stress-strain and thermal behaviors of CNT-reinforced composites. These findings underscored the importance of distribution strategies in enhancing mechanical and thermal performance. FG-CNTRC plates are particularly sensitive to temperature changes, which can significantly influence their mechanical behavior. Wang et al. (2018) analyzed thermal vibration and bending in FG-CNTRC shells, emphasizing how thermal gradients can impact structural stability. Uymaz and Uymaz (2023) performed 3D thermal vibration analyses and identified the ways that temperature distributions affect natural frequencies. Mehar et al. (2015) explored the effects of thermal gradients on bending stiffness, revealing that increased temperatures decrease stiffness while raising vibrational frequencies. The impact of mechanical loads combined with temperature variations was investigated by Foroutan et al. (2021), who identified the optimal CNTRC distribution for improved buckling resistance and free vibration response under joint loads. Hygrothermal vibration analysis conducted by Zaitoun et al. (2023) demonstrated intensified stress responses in FG-CNTRCs in response to changing environmental conditions. Research by Dey and Bandyopadhyay (2023) and Kiani (2016) examined the free vibration characteristics of porous and spherical FG-CNT composites, respectively. These studies highlighted the need for incorporating both thermal and mechanical factors into material design. Sobhy and Al Mukahal (2023) expanded these studies to FG-CNTRC sandwich plates under magnetic control, demonstrating enhanced stability in dynamic scenarios. Boundary conditions are vital for determining the mechanical response of FG-CNTRC plates. Ansari et al. (2020) and Quoc et al. (2019) analyzed buckling and vibrational behaviors under varying conditions, showing that clamped edges provide more resistance compared to simply supported boundaries. Rout and Hota (2023) and Kallannavar et al. (2022) studied the impacts of moisture and temperature on laminated plates, revealing significant effects on stability and stiffness. Bowles and Tompkins (1989) contributed early foundational insights into the thermal expansion coefficients of CNT composites, which remain critical for understanding boundary condition responses. Aspect ratios, including length-to-width and width-to-thickness ratios, are also essential design considerations. Lazar et al. (2023) and Mehar et al. (2015) noted that changing aspect ratios can optimize stiffness and bending characteristics, aiding in the creation of lightweight yet strong structures. Advanced numerical and analytical methods have been developed for analyzing FG-CNTRC plates. Liu et al. (2020) employed isogeometric analysis to achieve high accuracy in evaluating bending and vibration. In addition, Guo et al. (2021) and Guo et al. (2019) utilized deep learning-based energy techniques for bending and buckling, showcasing the effectiveness of advanced computational approaches. Meshfree methods, as used by Shams et al. (2015), provide a versatile strategy for examining large deformations in FG-CNTRCs. Early research by Di Sciuva and Sorrenti (2019) offered crucial insights into the mechanical properties of CNT-polymer composites and vibration behavior through refined zigzag theories. Chalak et al. (2021) further studied hygrothermal effects in FG beams using refined zigzag theories, revealing that moisture and temperature significantly impact vibrational stability. Van Do and Lee (2022) investigated the nonlinear bending behavior of CNT-reinforced composite plates under thermal and combined thermal-mechanical loading. Using an isogeometric analysis framework along with Quasi-3D shear deformable plate theory, they demonstrated the influence of CNT volume fractions, distribution patterns, and boundary conditions on bending performance. Their findings provide valuable insights into thermo-mechanical coupling effects and establish benchmark solutions for advanced nanocomposite materials.

Despite extensive research, significant gaps remain in the bending analysis of FG-CNTRC plates subjected to non-uniform CNT distributions. To remedy this shortcoming, this study introduces the first thorough bending analysis of both linear and non-linear functionally graded carbon nanotube-reinforced composite (CNT-RC) plates by incorporating the effects of temperature-dependent material characteristics. Utilizing first-order shear deformation theory (FSDT), the governing equations are formulated and solved using the finite element method to assess the central deflection of the nanocomposite plates. The analysis carefully investigates the influences of plate geometry (length- to-width and width- to-thickness ratios), CNT volume fraction, boundary conditions, along with both linear and nonlinear CNT distributions on the central deflection of functionally graded CNT-RC plates. This research provides valuable insights for the design and optimization of functionally graded CNT-RC materials across various engineering applications.

2. MODELING APPROACH

2.1. Constituent Properties of the CNT-Reinforced Composite Plate

Attention is directed toward a composite plate enhanced with carbon nanotubes (CNTs), where an isotropic polymer matrix is reinforced by nanoscale CNT fillers. Figure 1 illustrates the plate, characterized by a length denoted as a, a width represented by b, and a thickness expressed as h, all defined within a rectangular coordinate framework(x, y, z) . It is segmented into NL layers, all possessing equal thickness. The volume fraction of CNTs in every layer can either be uniform or change gradually throughout the thickness direction, adhering to three separates functionally graded (FG) distribution patterns, as detailed by Chiker et al. (2020).

$$\text{UD:} \quad V_{CNT}^{(k)} = V_{CNT}^{*} \tag{1a}$$

$$\text{FG-X:} \quad V_{CNT}^{(k)} = (1+Pin)\left(\frac{|2k-N_L-1|}{N_L}\right)^{Pin} V_{CNT}^{*} \tag{1b}$$

$$\text{FG-O:} \quad V_{CNT}^{(k)} = (1+Pin)\left(1-\frac{|2k-N_L-1|}{N_L}\right)^{Pin} V_{CNT}^{*} \tag{1c}$$

$$\text{FG-V:} \quad V_{CNT}^{(k)} = (1+Pin)\left(\frac{k-0.5}{N_L}\right)^{Pin} V_{CNT}^{*} \tag{1e}$$

The parameter is the power-law index that controls both linear ($Pin = 1$) and nonlinear ($Pin \neq 1$) distributions. The volume fraction of carbon nanotubes (CNTs) can be represented as follows:

$$V_{CNT}^{*} = \frac{w^{CNT}}{(1-w^{CNT})(\rho^{CNT}/\rho^{m}) + w^{CNT}} \tag{2}$$

w^{CNT} indicates the weight fraction of carbon nanotubes (CNTs), whereas ρ^{CNT} and ρ^{m} refer, respectively, to the density values associated with the carbon nanotube phase and the host matrix material.

The relationship between the matrix volume fraction $V_m^{(k)}$ and the CNT volume proportion $V_{CNT}^{(k)}$ is as follows:

$$V_{CNT}^{(k)} + V_m^{(k)} = 1 \tag{3}$$

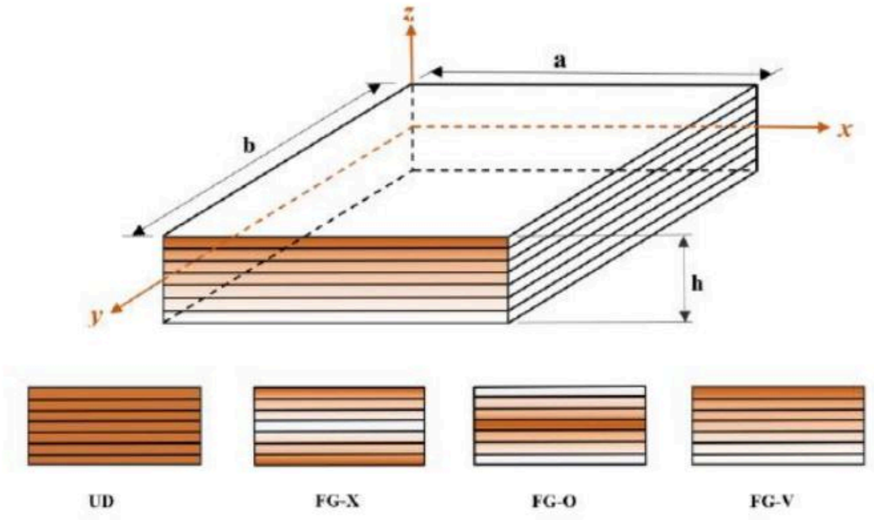

Figure 1. Structure and CNT dispersion profiles within the composite plate.

Journal of Information Systems Engineering and Management
2025, 10(1)
e-ISSN: 2468-4376
https://www.jisem-journal.com/
Research Article

Employing the mixture rule, the elastic modulus of the nanocomposite plates along the longitudinal and transverse axes, as well as the shear modulus in the longitudinal plane, are determined as outlined below, per references Duc 2017; Golmakani, Rahimi, and Sadeghian 2021; Z. Wang and Shen 2012; Zhang, Song, and Liew 2015:

$$E_{11}^{(k)} = \eta_1 V_{CNT}^{(k)} E_{11}^{CNT} + V_m^{(k)} E^m \tag{4a}$$

$$\frac{\eta_2}{E_{22}^{(k)}} = \frac{V_{CNT}^{(k)}}{E_{22}^{CNT}} + \frac{V_m^{(k)}}{E^m} \tag{4b}$$

$$\frac{\eta_3}{G_{12}^{(k)}} = \frac{V_{CNT}^{(k)}}{G_{12}^{CNT}} + \frac{V_m^{(k)}}{G^m} \tag{4c}$$

$$\nu_{12}^{(k)} = V_{CNT}^{*} \nu_{12}^{CNT} + V_m^{(k)} \nu^m \tag{4d}$$

$$\rho^{(k)} = V_{CNT}^{*} \rho^{CNT} + V_m^{(k)} \rho^m \tag{4e}$$

The characterization of the materials includes essential mechanical and physical properties. For carbon nanotubes (CNTs), the parameters involve stiffness along different directions (E_{11}, E_{22}), shear stiffness parameter (G_{12}), Poisson's ratio (ν_{12}), and volumetric density (ρ^{CNT}).Likewise, the matrix material is defined by its elastic modulus (E_m), shear stiffness parameter (G_m), Poisson's ratio (ν_m), and volumetric density (ρ_m).The quantities η_i(where $i=1, 2, 3$) representing the effectiveness of carbon nanotube reinforcement, are provided in Table 1, as originally published by Zhu et al. (2012).

Table 1:CNT Efficiency parameter values.

V_{CNT}^{*}	η_1	η_2	η_3
0.11	0.149	0.934	0.934
0.14	0.150	0.941	0.941
0.17	0.149	1.381	1.381

The thermally sensitive characteristics of the designated single-walled carbon nanotube with chirality index (10,10), as detailed in Table 2, are directly sourced from the article by Zhu et al. (2012).

Table 2:Thermo-mechanical characteristics of a single-walled carbon nanotube with chirality (10,10), defined by an effective wall thickness of 0.067 nm, an outer radius of 0.68 nm, a length of 9.26 nm, considering temperature variation.

Temperature (K)	E_{11}^{CNT}(TPa)	E_{22}^{CNT}(TPa)	G_{12}^{CNT} (TPa)	α_{11}^{CNT}	α_{22}^{CNT}
300	5.6466	7.0800	1.9445	3.4584	5.1682
500	5.5308	6.9348	1.9643	4.5361	5.0189
700	5.4744	6.8641	1.9644	4.6677	4.8943

2.2.Core equations of the model

The formulation originates from first-order shear deformation theory (FSDT), and as articulated by Reddy (2004), the kinematic behavior of the CNTRC panel is expressed through the following relations:

$$\begin{cases} u(x,y,z) = u_0(x,y) + z\theta_x(x,y) \\ v(x,y,z) = v_0(x,y) + z\theta_y(x,y) \\ w(x,y,z) = w_0(x,y) \end{cases} \tag{5}$$

The functions$u_0(x,y)$, $v_0(x,y)$, and $w_0(x,y)$represent the displacements of the central surface of the plate in the x, y, and z directions, respectively. Moreover, the rotations of the normal to the mid-surface about the x- and y-axes are denoted by$\theta_x(x,y)$and $\theta_y(x,y)$.

$$\begin{Bmatrix} \varepsilon_x^{(k)} \\ \varepsilon_y^{(k)} \\ \gamma_{xy}^{(k)} \\ \gamma_{yz}^{(k)} \\ \gamma_{xz}^{(k)} \end{Bmatrix} = \begin{Bmatrix} \varepsilon_x^{(0)} \\ \varepsilon_y^{(0)} \\ \gamma_{xy}^{(0)} \\ \gamma_{yz}^{(0)} \\ \gamma_{xz}^{(0)} \end{Bmatrix} + \begin{Bmatrix} \varepsilon_x^{(1)} \\ \varepsilon_y^{(1)} \\ \gamma_{xy}^{(1)} \\ \gamma_{yz}^{(1)} \\ \gamma_{xz}^{(1)} \end{Bmatrix} = \begin{Bmatrix} \dfrac{\partial u_0}{\partial x} \\ \dfrac{\partial v_0}{\partial y} \\ \dfrac{\partial u_0}{\partial y} + \dfrac{\partial v_0}{\partial x} \\ \dfrac{\partial w_0}{\partial y} + \theta_y \\ \dfrac{\partial w_0}{\partial x} + \theta_x \end{Bmatrix} + \begin{Bmatrix} \dfrac{\partial \theta_x}{\partial x} \\ \dfrac{\partial \theta_y}{\partial y} \\ \dfrac{\partial \theta_x}{\partial y} + \dfrac{\partial \theta_y}{\partial x} \\ 0 \\ 0 \end{Bmatrix} \tag{6}$$

The following expressions describe the linear elastic relationship that links stress to strain within the material.

$$\begin{Bmatrix} \sigma_x^{(k)} \\ \sigma_y^{(k)} \\ \tau_{xy}^{(k)} \\ \tau_{yz}^{(k)} \\ \tau_{xz}^{(k)} \end{Bmatrix} = \begin{bmatrix} Q_{11}^{(k)} & Q_{12}^{(k)} & 0 & 0 & 0 \\ Q_{12}^{(k)} & Q_{22}^{(k)} & 0 & 0 & 0 \\ 0 & 0 & Q_{44}^{(k)} & 0 & 0 \\ 0 & 0 & 0 & Q_{55}^{(k)} & 0 \\ 0 & 0 & 0 & 0 & Q_{66}^{(k)} \end{bmatrix} \begin{Bmatrix} \varepsilon_x^{(k)} \\ \varepsilon_y^{(k)} \\ \gamma_{xy}^{(k)} \\ \gamma_{yz}^{(k)} \\ \gamma_{xz}^{(k)} \end{Bmatrix} \tag{7}$$

With the matrix elements defined as:

$$Q_{11}^{(k)} = \frac{E_{11}^{(k)}}{1-\nu_{12}^{(k)}\nu_{21}^{(k)}},\ Q_{22}^{(k)} = \frac{E_{22}^{(k)}}{1-\nu_{12}^{(k)}\nu_{21}^{(k)}},\ Q_{12}^{(k)} = \frac{\nu_{21}^{(k)}E_{11}^{(k)}}{1-\nu_{12}^{(k)}\nu_{21}^{(k)}},\ Q_{44}^{(k)} = G_{23}^{(k)},\ Q_{55}^{(k)} = G_{13}^{(k)},\ Q_{66}^{(k)} = G_{12}^{(k)} \tag{8}$$

The relationships (constitutive equations) connecting the internal forces (N_x, N_y, N_{xy}) within the plane, shear stresses (Q_x, Q_y), and moment distributions (M_x, M_y, M_{xy}) are linked to their corresponding strain responses are expressedas follows:

$$\begin{Bmatrix} N_x \\ N_y \\ N_{xy} \end{Bmatrix} = \begin{bmatrix} A_{11} & A_{12} & A_{16} \\ A_{12} & A_{22} & A_{26} \\ A_{16} & A_{26} & A_{66} \end{bmatrix} \begin{Bmatrix} \varepsilon_x^{(0)} \\ \varepsilon_y^{(0)} \\ \varepsilon_{xy}^{(0)} \end{Bmatrix} + \begin{bmatrix} B_{11} & B_{12} & B_{16} \\ B_{12} & B_{22} & B_{26} \\ B_{16} & B_{26} & B_{66} \end{bmatrix} \begin{Bmatrix} \varepsilon_x^{(1)} \\ \varepsilon_y^{(1)} \\ \varepsilon_{xy}^{(1)} \end{Bmatrix} \tag{9}$$

$$\begin{Bmatrix} M_x \\ M_y \\ M_{xy} \end{Bmatrix} = \begin{bmatrix} B_{11} & B_{12} & B_{16} \\ B_{12} & B_{22} & B_{26} \\ B_{16} & B_{26} & B_{66} \end{bmatrix} \begin{Bmatrix} \varepsilon_x^{(0)} \\ \varepsilon_y^{(0)} \\ \varepsilon_{xy}^{(0)} \end{Bmatrix} + \begin{bmatrix} D_{11} & D_{12} & D_{16} \\ D_{12} & D_{22} & D_{26} \\ D_{16} & D_{26} & D_{66} \end{bmatrix} \begin{Bmatrix} \varepsilon_x^{(1)} \\ \varepsilon_y^{(1)} \\ \varepsilon_{xy}^{(1)} \end{Bmatrix} \tag{5}$$

$$\begin{Bmatrix} Q_x \\ Q_y \end{Bmatrix} = \frac{5}{6} \begin{bmatrix} F_{44} & F_{45} \\ F_{45} & F_{55} \end{bmatrix} \begin{Bmatrix} \gamma_{yz}^{(0)} \\ \gamma_{xz}^{(0)} \end{Bmatrix} \tag{6}$$

The plate's stiffness elements are defined as:

$$(A_{ij},B_{ij},D_{ij})=\sum_{k=1}^{N_L}\int_{Z_k}^{Z_{k+1}} Q_{ij}^{(k)}(1,z,z^2)dz\,,\ \ (i,\ j=1,2,6) \tag{7}$$

$$F_{ij}=\sum_{k=1}^{N_L}\int_{Z_k}^{Z_{k+1}} Q_{ij}^{(k)}dz\,,\ (i,\ j=1,2,6) \tag{8}$$

By combining the equations (9-11), we obtained:

$$\begin{Bmatrix} N \\ M \\ Q \end{Bmatrix}=\begin{bmatrix} A & B & 0 \\ B & D & 0 \\ 0 & 0 & F \end{bmatrix}\begin{Bmatrix} \varepsilon_0 \\ \kappa \\ \gamma \end{Bmatrix} \tag{9}$$

2.3. Finite element method

A nine-node quadrilateral element, constructed via isoparametric mapping, is employed to represent the spatial variation of displacements across the domain. Eachnode possesses five independent degrees of freedom: three displacements along the directional path of the x, y, and z axes, represented as u, v, and w,and two rotational components around the x and y axes, represented by θ_x and θ_y. The displacement formulation can be expressed mathematically as follows:

$$\begin{Bmatrix} u_0 \\ v_0 \\ w_0 \\ \theta_x \\ \theta_y \end{Bmatrix}=\sum_{i=1}^{9}\begin{bmatrix} N_i & 0 & 0 & 0 & 0 \\ 0 & N_i & 0 & 0 & 0 \\ 0 & 0 & N_i & 0 & 0 \\ 0 & 0 & 0 & N_i & 0 \\ 0 & 0 & 0 & 0 & N_i \end{bmatrix}\begin{Bmatrix} u_{0i} \\ v_{0i} \\ w_{0i} \\ \theta_{xi} \\ \theta_{yi} \end{Bmatrix} \tag{15}$$

$N_i$signifies the shape functions used for interpolation.

The equation (15) can be expressed in a more condensed manner, as shown:

$$\{\delta\}=[N]\{\delta_e\} \tag{16}$$

The functional connection between elementary deformation and positional change is characterized by:

$$\begin{Bmatrix} \varepsilon_{0x} \\ \varepsilon_{0y} \\ \gamma_{0xy} \\ \kappa_x \\ \kappa_y \\ \kappa_{xy} \\ \gamma_{xz} \\ \gamma_{yz} \end{Bmatrix}=\sum_{i=1}^{9}\begin{bmatrix} \partial N_i/\partial x & 0 & 0 & 0 & 0 \\ 0 & \partial N_i/\partial y & 0 & 0 & 0 \\ \partial N_i/\partial y & \partial N_i/\partial x & 0 & 0 & 0 \\ 0 & 0 & 0 & \partial N_i/\partial x & 0 \\ 0 & 0 & 0 & 0 & \partial N_i/\partial y \\ 0 & 0 & 0 & \partial N_i/\partial y & \partial N_i/\partial x \\ 0 & 0 & \partial N_i/\partial x & N_i & 0 \\ 0 & 0 & \partial N_i/\partial y & 0 & N_i \end{bmatrix}\begin{Bmatrix} u_{0i} \\ v_{0i} \\ w_{0i} \\ \theta_{xi} \\ \theta_{yi} \end{Bmatrix} \tag{17}$$

Equation 17 is transformed into a compact matrix notation, given by:

$$\{\varepsilon\}=[B]\{\varepsilon_e\} \tag{18}$$

Employing Hamilton's variational approach, the governing finite element equilibrium equation for bending behavior is established as:

$$[K]\{\delta\} = F \tag{19}$$

Within the given equation, [K] denotes the assembled stiffness matrix.

The mathematical representation of the elementary stiffness matrices $[K_e]$ is provided as:

$$[K_e] = \iint [B]^T [C][B]\,dxdy \tag{20}$$

Matrice [C] represent, the elasticity of the material, and are formulated as:

$$[C] = \begin{bmatrix} A & B & 0 \\ B & D & 0 \\ 0 & 0 & F \end{bmatrix} \tag{21}$$

3. NUMERICAL FINDINGS AND INTERPRETATION

3.1. Comparison studies:

To establish the credibility of the mathematical models, a benchmarking analysis was performed. This involved a direct comparison of the computational outcomes for CNT-reinforced composites (CNT-RC) with established data from existing scholarly publications. The comparison study investigated SSSS CNT-RC plates, focusing on varied width- to-thickness proportions and distinct CNT distribution (FG-O, FG-V, UD, FG-X). Table 3 captures the changes in elastic characteristics of CNT-RC structures. Table 4 showcases the defining material properties of the PmPV matrix, formally known as poly(m-phenylenevinylene)-co-(2.5-dioctoxy-p-phenylene).Table 5 presents the efficiency parameters for varying values of V_{CNT}^*. The comparison is performed specifically for a fixed CNT volume fraction maintained at 0.11.

Table 3: Elastic properties of the CNT reinforced composite (CNT-RC).

E_{11}^{CNT}	E_{22}^{CNT}	G_{12}^{CNT}	α_{11}^{CNT}	α_{22}^{CNT}
5.6466 TPa	7.0800 TPa	1.9445 TPa	3.4584 (10^{-6}/K)	5.1682 (10^{-6}/K)

Table 4: PmPV Matrix material properties.

Property	Value	Units
Density, ρ^m	1150	Kg/m3
Poisson's Ratio, ν^m	0.34	1
Young's Modulus, E^m	2.1	GPa

Table 5: Efficiency parameters for varying V_{CNT}^* Values.

V_{CNT}^*	η_1	η_2	η_3
0.11	0.149	0.934	0.934
0.14	0.150	0.941	0.941

0.17	0.149	1.381	1.381

A comparative analysis of the dimensionless midpoint displacement ($\bar{\omega} = -\omega/h$) of CNT-RC plates with simply supported edges (SSSS), subjected to a uniformly applied load ($q_0 = -1.0 \times 10^{-5}\,N/m^2$). was conducted in relation to the outcomes provided by Zhu et al. (2012), which are outlined in Table 6. A constant temperature of 300K (room temperature) was maintained during the numerical analyses. The observed concordance highlights the reliability of the outcomes obtained in the present study for CNT-RC plates that incorporate a functionally graded nanoscale reinforcement scheme.

Table 6: Comparison of Non-dimensional midpoint displacement for simply supported CNT-reinforced composite plates under uniform load with Zhu et al. (2012).

		a/b=1			
		b/h=10		b/h=50	
V_{CNT}^{*}	Distribution patterns	Present	Ref. Zhu et al. (2012).	Present	Ref. Zhu et al. (2012).
0.11	UD	0.3736×10^{-02}	0.3739×10^{-02}	1.157	1.155
	FG-V	0.4456×10^{-02}	0.4466×10^{-02}	1.651	1.653
	FG-O	0.5195×10^{-02}	0.5230×10^{-02}	2.139	2.157
	FG-X	0.3179×10^{-02}	0.3177×10^{-02}	0.7890	0.7900

3.2. Parametric studies:

This section explores how various factors—such as the proportion between the plate's length and width, the proportion between its width and thickness, the manner in which its edges are supported, the CNT volume fraction, and both linear and nonlinear CNT distributions—affect the natural vibration response of composite plates strengthened with carbon nanotubes.The modeled nanocomposite plates, exhibiting a functionally graded structure, consist of a poly(m-phenylenevinylene)-co-[(2,5-dioctoxy-p-phenylene) vinylene] (PmPV) base matrix, reinforced with armchair-structured single-walled carbon nanotubes of the (10, 10) type. The mechanical response under elastic deformation of these CNTs has been listed in Table 7. The temperature sensitivity of the PmPV matrix properties is taken into account, with the relevant data listed in Table 8.

Table 7: Material parameters of the (10,10) single-walled carbon nanotube (SWCNT), including length (L = 9.26 nm), radius (R = 0.68 nm), wall thickness (h = 0.067 nm), and effective volume fraction (V_{CNT}^{*} = 0.175), based on Zhu et al. (2012).

Temperature (K)	E_{22}^{CNT}(TPa)	E_{22}^{CNT}(TPa)	G_{12}^{CNT} (TPa)	$\alpha_{11}^{CNT}(10^{-6}/K)$	$\alpha_{12}^{CNT}(10^{-6}/K)$
300	5.6466	7.0800	1.9445	3.4584	5.1682
500	5.5308	6.9348	1.9643	4.5361	5.0189
700	5.4744	6.8641	1.9644	4.6677	4.8943

Table 8: Temperature-Dependent PmPV Matrix Material Properties.

Property	Value	Units
ν^m	0.34	1
ρ^m	1150	Kg/m3
E^m	$(3.51\text{-}0.0047\times T)$	GPa

The numerical analysis investigates the behavior of plates with four distinct carbon nanotube (CNT) reinforcement configurations (UD, FG-V, FG-O, and FG-X) across different edge fixation types(CCCC, SSSS, CCSS, CSCS, CSSS, CCCS). The corresponding CNT volume fractions and their impact on performance metrics are detailed in Table 5. To accurately represent the gradual change in CNT concentration throughout the plate's thickness, a 20-layer discretization (N_L = 20) is employed. The study examines the effects of varying proportions between width and thickness (b/h = 10, 20, 50) and aspect ratios (a/b = 1, 1.5, 2) on the dimensionless central deflection, which is determined using the following

mathematical expression: $\bar{\omega} = \omega/h$. All simulations are conducted across various thermal environments, specifically at 300K, 500K, and 700K.

Table 9 presents the non-dimensional central deflection of simply-supported CNT-reinforced composite (CNT-RC) plates subjected to a uniform distributed loading, with a constant width-to-thickness ratio of a/b=1 and a CNT volume fraction of 0.11. As the width-to-thickness ratio increases, the non-dimensional central deflection of the plates also increases, indicating a decrease in the overall stiffness of the plates as their width becomes more significant relative to their thickness. Table 9 also reveals the significant influence of CNT distribution patterns on the deflection behavior. Among the different distribution patterns considered, the FG-O pattern yields the highest non-dimensional central deflection, while the FG-X pattern leads to the lowest. This suggests that the distribution of CNTs has a critical effect on the stiffness of the nanocomposite plates. Specifically, the FG-X pattern, where CNTs are more concentrated at the top and bottom surfaces of the plate, results in a stiffer plate, reducing the central deflection. Furthermore, the effect of power law index variations is examined in the data. As the power law index increases from 0 to 1.8, the non-dimensional central deflection increases for the FG-O and FG-V patterns. However, the FG-X pattern exhibits a decrease in deflection as the index increases, while the UD pattern shows no variation in central deflection across different power law indexes. This behavior is explained by the different CNT distributions: in the FG-O pattern, CNTs are concentrated in the middle of the plate, leading to increased deflection as the index rises. For FG-V, CNTs are concentrated at the upper surface, and the increase in the power law index causes an increase in deflection. In contrast, for the FG-X pattern, where CNTs are concentrated at both the top and bottom surfaces, higher power law indexes result in stiffer plates with reduced deflection.

These findings underline the crucial role of both CNT distribution and power law index in tuning the mechanical properties of CNT-RC plates, offering insights into the optimal design for enhanced stiffness.

Table 9: Non-dimensional central deflection$\bar{\omega} = -\omega/h$ of simply-supported CNT-RC plates subjected to a uniform distributed loading$q_0 = -1.0 \times 10^{-5}\text{N/m}^2$, under the effects of different width-to-thickness ratios, CNT distribution patterns, and power law indexes. With fixed a/b=1, SSSS, V^*_{CNT} = 0.11and T=300k.

		P_{in}					
b/h	Distribution Patterns	0	0.4	0.8	1	1.4	1.8
	UD	0.3736×10^{-02}	0.3736×10^{-02}	0.3736×10^{-02}	0.3736×10^{-02}	0.3736×10^{-02}	0.3736×10^{-02}

Journal of Information Systems Engineering and Management
2025, 10(1)
e-ISSN: 2468-4376
https://www.jisem-journal.com/

Research Article

10	FG-V	0.3736×10^{-02}	0.3979×10^{-02}	0.4290×10^{-02}	0.4456×10^{-02}	0.4801×10^{-02}	0.5153×10^{-02}
	FG-O	0.3736×10^{-02}	0.4265×10^{-02}	0.4875×10^{-02}	0.5195×10^{-02}	0.5850×10^{-02}	0.6513×10^{-02}
	FG-X	0.3736×10^{-02}	0.3423×10^{-02}	0.3243×10^{-02}	0.3179×10^{-02}	0.3080×10^{-02}	0.3007×10^{-02}
20	UD	0.3631×10^{-01}	0.3631×10^{-01}	0.3631×10^{-01}	0.3631×10^{-01}	0.3631×10^{-01}	0.3631×10^{-01}
	FG-V	0.3631×10^{-01}	0.4046×10^{-01}	0.4583×10^{-01}	0.4873×10^{-01}	0.5474×10^{-01}	0.6090×10^{-01}
	FG-O	0.3631×10^{-01}	0.4527×10^{-01}	0.5563×10^{-01}	0.6107×10^{-01}	0.7222×10^{-01}	0.8353×10^{-01}
	FG-X	0.3631×10^{-01}	0.3110×10^{-01}	0.2814×10^{-01}	0.2710×10^{-01}	0.2552×10^{-01}	0.2439×10^{-01}
50	UD	1.157	1.157	1.157	1.157	1.157	1.157
	FG-V	1.157	1.321	1.535	1.651	1.891	2.138
	FG-O	1.157	1.512	1.923	2.139	2.583	3.032
	FG-X	1.157	1.087	1.027	1.007	0.977	0.956

Table 10 presents the non-dimensional central deflection of simply-supported CNT-RC plates subjected to a uniform distributed loading, considering the effects of aspect ratio, CNT distribution patterns, and power law indexes. With a fixed aspect ratio b/h=10 and CNT volume fraction $V^*_{CNT} = 0.11$, the results show that as the aspect ratio increases from 1 to 2, the non-dimensional central deflection increases for all power law indexes and CNT distribution patterns, indicating a reduction in stiffness as the aspect ratio becomes larger. Among the various CNT distribution patterns, the FG-O pattern yields the highest non-dimensional central deflection, while the FG-X pattern produces the lowest deflection, suggesting that the FG-X pattern, where CNTs are concentrated at the top and bottom surfaces, results in a stiffer nanocomposite plate. The effect of varying the power law index from 0 to 1.8 shows that for the FG-O and FG-V patterns, the non-dimensional central deflection increases as the index increases, while for the FG-X pattern, the deflection decreases, and the UD pattern shows no variation. This is due to the same reason mentioned in the above paragraph.

Table 10: non-dimensional central deflection $\bar{\omega} = -\omega/h$ of simply-supported CNT-RC plates subjected to a uniform distributed loading $q_0 = -1.0\times10^{-5}\mathrm{N/m^2}$, under the effects of different aspect ratios, CNT distribution patterns, and power law indexes. With fixed b/h=10, SSSS, $V^*_{CNT} = 0.11$ and T=300k.

		P_{in}					
a/b	Distribution Patterns	0	0.4	0.8	1	1.4	1.8
1	UD	0.3736×10^{-02}	0.3736×10^{-02}	0.3736×10^{-02}	0.3736×10^{-02}	0.3736×10^{-02}	0.3736×10^{-02}
	FG-V	0.3736×10^{-02}	0.3979×10^{-02}	0.4290×10^{-02}	0.4456×10^{-02}	0.4801×10^{-02}	0.5153×10^{-02}

	FG-O	0.3736×10^{-02}	0.4265×10^{-02}	0.4875×10^{-02}	0.5195×10^{-02}	0.5850×10^{-02}	0.6513×10^{-02}
	FG-X	0.3736×10^{-02}	0.3423×10^{-02}	0.3243×10^{-02}	0.3179×10^{-02}	0.3080×10^{-02}	0.3007×10^{-02}
1.5	UD	0.1199×10^{-01}	0.1199×10^{-01}	0.1199×10^{-01}	0.1199×10^{-01}	0.1199×10^{-01}	0.1199×10^{-01}
	FG-V	0.1199×10^{-01}	0.1289×10^{-01}	0.1397×10^{-01}	0.1452×10^{-01}	0.1558×10^{-01}	0.1659×10^{-01}
	FG-O	0.1199×10^{-01}	0.1397×10^{-01}	0.1609×10^{-01}	0.1713×10^{-01}	0.1914×10^{-01}	0.2100×10^{-01}
	FG-X	0.1199×10^{-01}	0.1076×10^{-01}	0.1003×10^{-01}	0.9767×10^{-02}	0.9359×10^{-02}	0.9057×10^{-02}
2	UD	0.2537×10^{-01}	0.2537×10^{-01}	0.2537×10^{-01}	0.2537×10^{-01}	0.2537×10^{-01}	0.2537×10^{-01}
	FG-V	0.2537×10^{-01}	0.2703×10^{-01}	0.2883×10^{-01}	0.2967×10^{-01}	0.3116×10^{-01}	0.3242×10^{-01}
	FG-O	0.2537×10^{-01}	0.2909×10^{-01}	0.3270×10^{-01}	0.3435×10^{-01}	0.3727×10^{-01}	0.3969×10^{-01}
	FG-X	0.2537×10^{-01}	0.2286×10^{-01}	0.2131×10^{-01}	0.2073×10^{-01}	0.1982×10^{-01}	0.1913×10^{-01}

Table 11 presents the non-dimensional central deflection of simply-supported CNT-RC plates subjected to uniform distributed loading, considering the effects of CNT volume fraction, CNT distribution patterns, and power law indexes. With a/b=1 and b/h=10, as the CNT volume fraction increases from 0.11 to 0.17, the non-dimensional central deflection decreases for all CNT distribution patterns and power law indexes, indicating that a higher volume fraction of CNTs enhances the stiffness of the nanocomposite plates. Among the different CNT distribution patterns, the FG-O pattern results in the highest non-dimensional central deflection, while the FG-X pattern yields the lowest deflection, suggesting that a more concentrated CNT distribution at the top and bottom surfaces (as in the FG-X pattern) produces a stiffer plate. The effect of varying the power law index from 0 to 1.8 shows that the non-dimensional central deflection increases for the FG-O and FG-V patterns, decreases for the FG-X pattern, and remains unchanged for the UD pattern. As previously explained, this behavior is explained by the differing CNT distributions: in the FG-O pattern, CNTs are concentrated in the middle of the plate, while in FG-V, CNTs are concentrated at the upper surface, and in UD, the CNT volume fraction remains constant across the thickness of the plate.

Table 11: non-dimensional central deflection $\bar{\omega} = -\omega/h$ of simply-supported CNT-RC plates subjected to a uniform distributed loading $q_0 = -1.0 \times 10^{-5}\mathrm{N/m}^2$, under the effects of different CNT volume fractions, CNT distribution patterns, and power law indexes. With fixed a/b=1, b/h=10, SSSS and T=300k.

		P_{in}					
V_{CNT}^{*}	Distribution Patterns	0	0.4	0.8	1	1.4	1.8
0.11	UD	0.3736×10^{-02}	0.3736×10^{-02}	0.3736×10^{-02}	0.3736×10^{-02}	0.3736×10^{-02}	0.3736×10^{-02}
	FG-V	$0.3736\times10^{-}$	$0.3979\times10^{-}$	$0.4290\times10^{-}$	$0.4456\times10^{-}$	$0.4801\times10^{-}$	$0.5153\times10^{-}$

		02	02	02	02	02	02
	FG-O	0.3736×10^{-02}	0.4265×10^{-02}	0.4875×10^{-02}	0.5195×10^{-02}	0.5850×10^{-02}	0.6513×10^{-02}
	FG-X	0.3736×10^{-02}	0.3423×10^{-02}	0.3243×10^{-02}	0.3179×10^{-02}	0.3080×10^{-02}	0.3007×10^{-02}
0.14	UD	0.3295×10^{-02}	0.3295×10^{-02}	0.3295×10^{-02}	0.3295×10^{-02}	0.3295×10^{-02}	0.3295×10^{-02}
	FG-V	0.3295×10^{-02}	0.3490×10^{-02}	0.3741×10^{-02}	0.3876×10^{-02}	0.4159×10^{-02}	0.4449×10^{-02}
	FG-O	0.3295×10^{-02}	0.3722×10^{-02}	0.4220×10^{-02}	0.4483×10^{-02}	0.5028×10^{-02}	0.5589×10^{-02}
	FG-X	0.3295×10^{-02}	0.3041×10^{-02}	0.2893×10^{-02}	0.2840×10^{-02}	0.2755×10^{-02}	0.2691×10^{-02}
0.17	UD	0.2393×10^{-02}	0.2393×10^{-02}	0.2393×10^{-02}	0.2393×10^{-02}	0.2393×10^{-02}	0.2393×10^{-02}
	FG-V	0.2393×10^{-02}	0.2550×10^{-02}	0.2751×10^{-02}	0.2859×10^{-02}	0.3080×10^{-02}	0.3305×10^{-02}
	FG-O	0.2393×10^{-02}	0.2740×10^{-02}	0.3142×10^{-02}	0.3353×10^{-02}	0.3788×10^{-02}	0.4229×10^{-02}
	FG-X	0.2393×10^{-02}	0.2183×10^{-02}	0.2060×10^{-02}	0.2015×10^{-02}	0.1942×10^{-02}	0.1886×10^{-02}

Table 12 examines the non-dimensional central deflection of CNT-RC plates subjected to uniform distributed loading, considering various boundary condition combinations, CNT distribution patterns, and power law indexes. To improve clarity, a four-letter notation is used to specify the boundary conditions at each edge of the plate. For example, FSSC indicates that the plate is free (F) at the $x = 0$ edge, simply supported (S) at the $y = 0$ edge, simply supported (S) at the $x = a$ edge, and clamped (C) at the $y = b$ edge. With $a/b=1$, $b/h = 10$, and $V^*_{CNT} = 0.11$, the results indicate that the highest non-dimensional central deflection corresponds to the SSSS boundary condition, while the lowest occurs for the CCCC boundary condition, suggesting that plates with clamped edges are stiffer than those with simply-supported edges. Among the different CNT distribution patterns, the FG-O pattern results in the highest deflection, and the FG-X pattern gives the lowest, demonstrating that dispersing CNTs according to the FG-X pattern, which concentrates CNTs at the top and bottom layers, leads to a stiffer nanocomposite plate. The variation in power law index from 0 to 1.8 shows that for the FG-O and FG-V patterns, the non-dimensional central deflection increases with the power law index, while for the FG-X pattern, the deflection decreases, and for the UD pattern, the deflection remains unchanged, regardless of the boundary conditions. These trends reflect the different CNT distributions: FG-O concentrates CNTs in the middle, FG-V places them at the upper surface, and UD maintains a uniform distribution across the plate thicknes.

Table 12: non-dimensional central deflection$\bar{\omega} = -\omega/h$ of CNT-RC plates subjected to a uniform distributed loading$q_0 = -1.0\times10^{-5}\mathrm{N/m}^2$, under the effects of different boundary condition combinations, CNT distribution patterns, and power law indexes.With fixed a/b=1, b/h=10, $V^*_{CNT} = 0.11$ and T=300k.

		P_{in}					
BC	Distribution Patterns	0	0.4	0.8	1	1.4	1.8

SSSS	UD	0.3736×10^{-02}	0.3736×10^{-02}	0.3736×10^{-02}	0.3736×10^{-02}	0.3736×10^{-02}	0.3736×10^{-02}
	FG-V	0.3736×10^{-02}	0.3979×10^{-02}	0.4290×10^{-02}	0.4456×10^{-02}	0.4801×10^{-02}	0.5153×10^{-02}
	FG-O	0.3736×10^{-02}	0.4265×10^{-02}	0.4875×10^{-02}	0.5195×10^{-02}	0.5850×10^{-02}	0.6513×10^{-02}
	FG-X	0.3736×10^{-02}	0.3423×10^{-02}	0.3243×10^{-02}	0.3179×10^{-02}	0.3080×10^{-02}	0.3007×10^{-02}
CCCC	UD	0.2222×10^{-02}	0.2222×10^{-02}	0.2222×10^{-02}	0.2222×10^{-02}	0.2222×10^{-02}	0.2222×10^{-02}
	FG-V	0.2222×10^{-02}	0.2266×10^{-02}	0.2320×10^{-02}	0.2349×10^{-02}	0.2408×10^{-02}	0.2468×10^{-02}
	FG-O	0.2222×10^{-02}	0.2323×10^{-02}	0.2440×10^{-02}	0.2501×10^{-02}	0.2629×10^{-02}	0.2760×10^{-02}
	FG-X	0.2222×10^{-02}	0.2158×10^{-02}	0.2119×10^{-02}	0.2104×10^{-02}	0.2079×10^{-02}	0.2058×10^{-02}
CCSS	UD	0.2897×10^{-02}	0.2897×10^{-02}	0.2897×10^{-02}	0.2897×10^{-02}	0.2897×10^{-02}	0.2897×10^{-02}
	FG-V	0.2897×10^{-02}	0.2997×10^{-02}	0.3123×10^{-02}	0.3189×10^{-02}	0.3324×10^{-02}	0.3463×10^{-02}
	FG-O	0.2897×10^{-02}	0.3119×10^{-02}	0.3371×10^{-02}	0.3503×10^{-02}	0.3781×10^{-02}	0.4065×10^{-02}
	FG-X	0.2897×10^{-02}	0.2758×10^{-02}	0.2674×10^{-02}	0.2643×10^{-02}	0.2594×10^{-02}	0.2555×10^{-02}
CSCS	UD	0.2363×10^{-02}	0.2363×10^{-02}	0.2363×10^{-02}	0.2363×10^{-02}	0.2363×10^{-02}	0.2363×10^{-02}
	FG-V	0.2363×10^{-02}	0.2414×10^{-02}	0.2481×10^{-02}	0.2517×10^{-02}	0.2594×10^{-02}	0.2675×10^{-02}
	FG-O	0.2363×10^{-02}	0.2476×10^{-02}	0.2611×10^{-02}	0.2683×10^{-02}	0.2836×10^{-02}	0.2998×10^{-02}
	FG-X	0.2363×10^{-02}	0.2295×10^{-02}	0.2254×10^{-02}	0.2238×10^{-02}	0.2214×10^{-02}	0.2194×10^{-02}
CSSS	UD	0.2984×10^{-02}	0.2984×10^{-02}	0.2984×10^{-02}	0.2984×10^{-02}	0.2984×10^{-02}	0.2984×10^{-02}
	FG-V	0.2984×10^{-02}	0.3093×10^{-02}	0.3232×10^{-02}	0.3307×10^{-02}	0.3461×10^{-02}	0.3623×10^{-02}
	FG-O	0.2984×10^{-02}	0.3222×10^{-02}	0.3496×10^{-02}	0.3642×10^{-02}	0.3951×10^{-02}	0.4271×10^{-02}
	FG-X	0.2984×10^{-02}	0.2837×10^{-02}	0.2750×10^{-02}	0.2717×10^{-02}	0.2666×10^{-02}	0.2627×10^{-02}

CCCS	UD	0.2322×10-02	0.2322×10-02	0.2322×10-02	0.2322×10-02	0.2322×10-02	0.2322×10-02
	FG-V	0.2322×10-02	0.2370×10-02	0.2431×10-02	0.2464×10-02	0.2534×10-02	0.2606×10-02
	FG-O	0.2322×10-02	0.2430×10-02	0.2557×10-02	0.2626×10-02	0.2768×10-02	0.2917×10-02
	FG-X	0.2322×10-02	0.2254×10-02	0.2214×10-02	0.2198×10-02	0.2173×10-02	0.2153×10-02

Table 13 presents the non-dimensional central deflection of simply-supported CNT-RC plates subjected to uniform distributed loading, considering the effects of different temperatures for mechanical properties, CNT distribution patterns, and power law indexes. With a/b=1, b/h=10, and $V^*_{CNT} = 0.11$, as the temperature increases from 300 K to 700 K, the non-dimensional central deflection slightly increases for all CNT distribution patterns and power law indexes. This suggests that the stiffness of the plates decreases with rising temperature, although the change is modest. Among the CNT distribution patterns, the FG-O pattern results in the highest deflection, while the FG-X pattern yields the lowest, indicating that dispersing CNTs according to the FG-X pattern leads to a stiffer nanocomposite plate across all considered temperatures and power law indexes. As the power law index increases from 0 to 1.8, the non-dimensional central deflection increases for FG-O and FG-V patterns, decreases for the FG-X pattern, and remains unchanged for the UD pattern. These trends reflect the CNT distribution patterns: in FG-O, CNTs are concentrated in the middle, in FG-V, they are concentrated at the upper surface, and in UD, the CNTs are uniformly distributed across the plate thickness.

Table 13: non-dimensional central deflection $\bar{\omega} = -\omega/h$ of simply-supported CNT-RC plates subjected to a uniform distributed loading $q_0 = -1.0 \times 10^{-5} \mathrm{N/m^2}$, under the effects of different temperature for the mechanical properties, CNT distribution patterns, and power law indexes. With fixed a/b=1, b/h=10, SSSS and $V^*_{CNT} = 0.11$.

		P_{in}					
T(K)	Distribution Patterns	0	0.4	0.8	1	1.4	1.8
300	UD	0.3736×10-02	0.3736×10-02	0.3736×10-02	0.3736×10-02	0.3736×10-02	0.3736×10-02
	FG-V	0.3736×10-02	0.3979×10-02	0.4290×10-02	0.4456×10-02	0.4801×10-02	0.5153×10-02
	FG-O	0.3736×10-02	0.4265×10-02	0.4875×10-02	0.5195×10-02	0.5850×10-02	0.6513×10-02
	FG-X	0.3736×10-02	0.3423×10-02	0.3243×10-02	0.3179×10-02	0.3080×10-02	0.3007×10-02
500	UD	0.3770×10-02	0.3770×10-02	0.3770×10-02	0.3770×10-02	0.3770×10-02	0.3770×10-02
	FG-V	0.3770×10-02	0.4017×10-02	0.4333×10-02	0.4502×10-02	0.4852×10-02	0.5208×10-02
	FG-O	0.3770×10-02	0.4309×10-02	0.4929×10-02	0.5253×10-02	0.5917×10-02	0.6589×10-02
	FG-X	0.3770×10-	0.3452×10-	0.3269×10-	0.3203×10-	0.3102×10-	0.3027×10-

		02	02	02	02	02	02
700	UD	0.3786×10^{-02}	0.3786×10^{-02}	0.3786×10^{-02}	0.3786×10^{-02}	0.3786×10^{-02}	0.3786×10^{-02}
	FG-V	0.3786×10^{-02}	0.4035×10^{-02}	0.4353×10^{-02}	0.4523×10^{-02}	0.4875×10^{-02}	0.5234×10^{-02}
	FG-O	0.3786×10^{-02}	0.4329×10^{-02}	0.4953×10^{-02}	0.5280×10^{-02}	0.5948×10^{-02}	0.6624×10^{-02}
	FG-X	0.3786×10^{-02}	0.3465×10^{-02}	0.3280×10^{-02}	0.3214×10^{-02}	0.3112×10^{-02}	0.3037×10^{-02}

Table 14 presents the non-dimensional central deflection of simply-supported CNT-RC plates subjected to uniform distributed loading, considering the effects of temperature, CNT volume fractions, CNT distribution patterns, and power law indexes. With a/b=1 and b/h=10, as the temperature increases from 300 K to 700 K, the non-dimensional central deflection slightly increases for all CNT distribution patterns and power law indexes. This indicates that the plates become slightly less stiff with increasing temperature. On the other hand, as the CNT volume fraction increases from 0.11 to 0.17, the non-dimensional central deflection decreases for all considered temperatures, power law indexes, and CNT distribution patterns, suggesting that higher CNT content enhances the stiffness of the nanocomposite plates. Among the different CNT distribution patterns, the FG-O pattern leads to the highest deflection, while the FG-X pattern results in the lowest deflection, demonstrating that dispersing CNTs according to the FG-X pattern, which concentrates them at the top and bottom layers, results in a stiffer nanocomposite plate across all temperatures and power law indexes.

Table 14: non-dimensional central deflection $\bar{\omega} = -\omega/h$ of simply-supported CNT-RC plates subjected to a uniform distributed loading$q_0 = -1.0 \times 10^{-5}\,\mathrm{N/m^2}$, under the effects of different temperature for the mechanical properties, CNT volume fractions, CNT distribution patterns, and power law indexes.With fixed a/b=1, b/h=10, and SSSS.

			P_{in}					
T(K)	V_{CNT}^{*}	Distribution Patterns	0	0.4	0.8	1	1.4	1.8
300	0.11	UD	0.3736×10^{-02}	0.3736×10^{-02}	0.3736×10^{-02}	0.3736×10^{-02}	0.3736×10^{-02}	0.3736×10^{-02}
		FG-V	0.3736×10^{-02}	0.3979×10^{-02}	0.4290×10^{-02}	0.4456×10^{-02}	0.4801×10^{-02}	0.5153×10^{-02}
		FG-O	0.3736×10^{-02}	0.4265×10^{-02}	0.4875×10^{-02}	0.5195×10^{-02}	0.5850×10^{-02}	0.6513×10^{-02}
		FG-X	0.3736×10^{-02}	0.3423×10^{-02}	0.3243×10^{-02}	0.3179×10^{-02}	0.3080×10^{-02}	0.3007×10^{-02}
	0.14	UD	0.3295×10^{-02}	0.3295×10^{-02}	0.3295×10^{-02}	0.3295×10^{-02}	0.3295×10^{-02}	0.3295×10^{-02}
		FG-V	0.3295×10^{-02}	0.3490×10^{-02}	0.3741×10^{-02}	0.3876×10^{-02}	0.4159×10^{-02}	0.4449×10^{-02}
		FG-O	0.3295×10^{-02}	0.3722×10^{-02}	0.4220×10^{-02}	0.4483×10^{-02}	0.5028×10^{-02}	0.5589×10^{-02}

		FG-X	0.3295×10^{-02}	0.3041×10^{-02}	0.2893×10^{-02}	0.2840×10^{-02}	0.2755×10^{-02}	0.2691×10^{-02}
	0.17	UD	0.2393×10^{-02}	0.2393×10^{-02}	0.2393×10^{-02}	0.2393×10^{-02}	0.2393×10^{-02}	0.2393×10^{-02}
		FG-V	0.2393×10^{-02}	0.2550×10^{-02}	0.2751×10^{-02}	0.2859×10^{-02}	0.3080×10^{-02}	0.3305×10^{-02}
		FG-O	0.2393×10^{-02}	0.2740×10^{-02}	0.3142×10^{-02}	0.3353×10^{-02}	0.3788×10^{-02}	0.4229×10^{-02}
		FG-X	0.2393×10^{-02}	0.2183×10^{-02}	0.2060×10^{-02}	0.2015×10^{-02}	0.1942×10^{-02}	0.1886×10^{-02}
500	0.11	UD	0.3770×10^{-02}	0.3770×10^{-02}	0.3770×10^{-02}	0.3770×10^{-02}	0.3770×10^{-02}	0.3770×10^{-02}
		FG-V	0.3770×10^{-02}	0.4017×10^{-02}	0.4333×10^{-02}	0.4502×10^{-02}	0.4852×10^{-02}	0.5208×10^{-02}
		FG-O	0.3770×10^{-02}	0.4309×10^{-02}	0.4929×10^{-02}	0.5253×10^{-02}	0.5917×10^{-02}	0.6589×10^{-02}
		FG-X	0.3770×10^{-02}	0.3452×10^{-02}	0.3269×10^{-02}	0.3203×10^{-02}	0.3102×10^{-02}	0.3027×10^{-02}
	0.14	UD	0.3323×10^{-02}	0.3323×10^{-02}	0.3323×10^{-02}	0.3323×10^{-02}	0.3323×10^{-02}	0.3323×10^{-02}
		FG-V	0.3323×10^{-02}	0.3521×10^{-02}	0.3776×10^{-02}	0.3914×10^{-02}	0.4201×10^{-02}	0.4496×10^{-02}
		FG-O	0.3323×10^{-02}	0.3758×10^{-02}	0.4264×10^{-02}	0.4532×10^{-02}	0.5086×10^{-02}	0.5654×10^{-02}
		FG-X	0.3323×10^{-02}	0.3064×10^{-02}	0.2914×10^{-02}	0.2859×10^{-02}	0.2773×10^{-02}	0.2707×10^{-02}
	0.17	UD	0.2415×10^{-02}	0.2415×10^{-02}	0.2415×10^{-02}	0.2415×10^{-02}	0.2415×10^{-02}	0.2415×10^{-02}
		FG-V	0.2415×10^{-02}	0.2575×10^{-02}	0.2780×10^{-02}	0.2889×10^{-02}	0.3114×10^{-02}	0.3341×10^{-02}
		FG-O	0.2415×10^{-02}	0.2769×10^{-02}	0.3177×10^{-02}	0.3392×10^{-02}	0.3834×10^{-02}	0.4281×10^{-02}
		FG-X	0.2415×10^{-02}	0.2202×10^{-02}	0.2076×10^{-02}	0.2030×10^{-02}	0.1957×10^{-02}	0.1899×10^{-02}
700	0.11	UD	0.3786×10^{-02}	0.3786×10^{-02}	0.3786×10^{-02}	0.3786×10^{-02}	0.3786×10^{-02}	0.3786×10^{-02}
		FG-V	0.3786×10^{-02}	0.4035×10^{-02}	0.4353×10^{-02}	0.4523×10^{-02}	0.4875×10^{-02}	0.5234×10^{-02}
		FG-O	0.3786×10^{-02}	0.4329×10^{-02}	0.4953×10^{-02}	0.5280×10^{-02}	0.5948×10^{-02}	0.6624×10^{-02}

		FG-X	0.3786×10^{-02}	0.3465×10^{-02}	0.3280×10^{-02}	0.3214×10^{-02}	0.3112×10^{-02}	0.3037×10^{-02}
	0.14	UD	0.3336×10^{-02}	0.3336×10^{-02}	0.3336×10^{-02}	0.3336×10^{-02}	0.3336×10^{-02}	0.3336×10^{-02}
		FG-V	0.3336×10^{-02}	0.3535×10^{-02}	0.3793×10^{-02}	0.3931×10^{-02}	0.4220×10^{-02}	0.4517×10^{-02}
		FG-O	0.3336×10^{-02}	0.3774×10^{-02}	0.4284×10^{-02}	0.4554×10^{-02}	0.5112×10^{-02}	0.5684×10^{-02}
		FG-X	0.3336×10^{-02}	0.3075×10^{-02}	0.2923×10^{-02}	0.2867×10^{-02}	0.2781×10^{-02}	0.2715×10^{-02}
	0.17	UD	0.2425×10^{-02}	0.2425×10^{-02}	0.2425×10^{-02}	0.2425×10^{-02}	0.2425×10^{-02}	0.2425×10^{-02}
		FG-V	0.2425×10^{-02}	0.2587×10^{-02}	0.2793×10^{-02}	0.2903×10^{-02}	0.3129×10^{-02}	0.3358×10^{-02}
		FG-O	0.2425×10^{-02}	0.2782×10^{-02}	0.3194×10^{-02}	0.3410×10^{-02}	0.3854×10^{-02}	0.4305×10^{-02}
		FG-X	0.2425×10^{-02}	0.2211×10^{-02}	0.2084×10^{-02}	0.2037×10^{-02}	0.1963×10^{-02}	0.1905×10^{-02}

4. CONCLUSION:

In conclusion, this article presents a comprehensive bending analysis of functionally graded carbon nanotube-reinforced composite (CNT-RC) plates with temperature-dependent material properties. The study provides an in-depth exploration of both uniform and non-uniform (functionally graded) CNT distributions across the plate thickness, a novel approach that has not been extensively studied before. To account for the temperature and moisture dependence of the material properties, the extended rule of mixtures is employed to determine the effective properties of the CNT-RC. The governing equations, incorporating are derived using first-order shear deformation theory (FSDT) and solved through the finite element method (FEM). A validation study ensures the accuracy and reliability of the analytical and numerical approaches used in this research. The subsequent parametric study explores various factors that influence the bending behaviour of CNT-RC plates, including plate geometry (length- to-width and width- to-thickness ratios), boundary conditions, CNT volume fraction, and both linear and non-linear CNT distribution patterns. Below are the findings of this paper:

- Results show, that increasing the width- to-thickness ratio raises the deflection for all patterns. FG-O gives the highest deflection, while FG-X provides the lowest, with the power law index affecting FG-O and FG-V patterns more significantly.
- Findings indicate that, as the aspect ratio increases, deflection increases for all patterns. FG-O has the highest deflection, and FG-X the lowest. Higher power law indices increase deflection for FG-O and FG-V, while decreasing it for FG-X.
- It is observed that, increasing CNT volume fraction reduces deflection across all patterns. FG-O shows the highest deflection, and FG-X the lowest, with the power law index affecting FG-O and FG-V more, and FG-X less.
- The analysis demonstrates that, the SSSS boundary condition gives the highest deflection, and CCCC the lowest. FG-O leads to the highest deflection, while FG-X leads to the lowest. The power law index increases deflection for FG-O and FG-V, and decreases it for FG-X.

- The study reveals that, as temperature increases, deflection slightly increases. FG-O shows the highest deflection, and FG-X the lowest. The power law index increases deflection for FG-O and FG-V, and decreases it for FG-X.
- The observations show that, higher temperatures slightly increase deflection, while higher CNT volume fractions reduce deflection. FG-O gives the highest deflection, and FG-X the lowest, with the power law index influencing FG-O and FG-V patterns more.

REFERENCES

[1] Ansari, R., R. Hassani, R. Gholami, and H. Rouhi. 2020. "Thermal Postbuckling Analysis of FG-CNTRC Plates with Various Shapes and Temperature-Dependent Properties Using the VDQ-FEM Technique." *Aerospace Science and Technology* 106: 106078. https://doi.org/10.1016/j.ast.2020.106078

[2] Bowles, D. E., and S. S. Tompkins. 1989. "Prediction of Coefficients of Thermal Expansion for Unidirectional Composites." *Journal of Composite Materials.* 23 (4): 370–388. https://doi.org/10.1177/002199838902300405

[3] Chalak, H. D., A. M. Zenkour, and A. Garg. 2021. "Free Vibration and Modal Stress Analysis of FG- CNTRC Beams under Hygrothermal Conditions Using Zigzag Theory." Mechanics Based Design of Structures and Machines. 51 (8): 4709–4730. https://doi.org/10.1080/15397734.2021.1977659

[4] Chiker, Y., M. Bachene, M. Guemana, B. Attaf, and S. Rechak. 2020. "Free Vibration Analysis of Multilayer Functionally Graded Polymer Nanocomposite Plates Reinforced with Nonlinearly Distributed Carbon-Based Nanofillers Using a Layer-Wise Formulation Model." *Aerospace Science and Technology.* 104: 105913. https://doi.org/10.1016/j.ast.2020.105913

[5] Dey, T., and T. Bandyopadhyay. 2023. "Free Vibration Response of Porous FGM Plates Using Finite Element Analysis in Thermal Environment." *Journal of Vibration Engineering & Technologies* 12 (3): 4593–4615. https://doi.org/10.1007/s42417-023-01139-5

[6] Di Sciuva, M., and M. Sorrenti. 2019. "Bending, Free Vibration and Buckling of Functionally Graded Carbon Nanotube-Reinforced Sandwich Plates, Using the Extended Refined Zigzag Theory." *Composite Structures* 227: 111324. https://doi.org/10.1016/j.compstruct.2019.111324

[7] Duc, N. D. 2017. "New Approach to Investigate Nonlinear Dynamic Response and Vibration of Imperfect Functionally Graded Carbon Nanotube Reinforced Composite Double Curved Shallow Shells Subjected to Blast Load and Temperature." *Aerospace Science and Technology* 1: 1-13. https://doi.org/10.1016/j.ast.2017.09.031

[8] Foroutan, K., E. Carrera, and H. Ahmadi. 2021. "Nonlinear Hygrothermal Vibration and Buckling Analysis of Imperfect FG-CNTRC Cylindrical Panels Embedded in Viscoelastic Foundations." European Journal of Mechanics-A/Solids 85: 104107. https://doi.org/10.1016/j.euromechsol.2020.104107

[9] Golmakani, M. E., E. Rahimi, and M. Sadeghian. 2021. "Large Deflection of Functionally Graded Carbon Nanotube Reinforced Composite Cylindrical Shell Exposed to Internal Pressure and Thermal Gradient." *Mathematical Methods in the Applied Sciences* 44 (17): 12654-12672.https://doi.org/10.1002/mma.7569

[10] Guo, H., X. Zhuang, and T. Rabczuk. 2019. "A Deep Collocation Method for the Bending Analysis of Kirchhoff Plate." Computers, Materials & Continua 59 (2): 433–456. https://doi.org/10.32604/cmc.2019.06660

[11] Guo, H., X. Zhuang, N. Alajlan, H. Zhu, and T. Rabczuk. 2021. "Deep Autoencoder Based Energy Method for the Bending, Vibration, and Buckling Analysis of Kirchhoff Plates with Transfer Learning." European Journal of Mechanics-A/Solids 87: 104225. https://doi.org/10.1016/j.euromechsol.2021.104225

[12] Iijima, S. 1991. "Helical Microtubules of Graphitic Carbon." Nature. 354: 56–58. https://doi.org/10.1038/354056a0

[13] Jiang, W., G. Ding, and H. Peng. 2009. "Measurement and Model on Thermal Conductivities of Carbon Nanotube Nanorefrigerants." *International Journal of Thermal Sciences* 48 (6): 1108–1115. https://doi.org/10.1016/j.ijthermalsci.2008.11.012

[14] Kallannavar, V., S. Kattimani, and H. Ramesh. 2022. "Influence of Temperature and Moisture on Free Vibration Behavior of Skew Laminated Composite Sandwich Panels with CNTRC Core." *International Journal of Structural Stability and Dynamics* 22 (08): 1–33. https://doi.org/10.1142/S0219455422500833

[15] Kiani, Y. 2016. "Free Vibration of FG-CNT Reinforced Composite Spherical Shell Panels Using Gram-Schmidt Shape Functions A Novel Class of Composites Known as Functionally Graded Carbon Nanotube Composites." *Composite Structures* 159: 368–381. https://doi.org/10.1016/j.compstruct.2016.09.079

[16] Lazar, M. E., M. Ezzraimi, R. Tiberkak, Y. Chiker, M. Bachene, and S. Rechak. 2023. "Vibration Analysis of Composite Plates Reinforced CNTs Using an Exponential Function Approach." *Materials Science Technology* 39 (17): 2680–2689. https://doi.org/10.1080/02670836.2023.2213975

[17] Liu, Z., C. Wang, G. Duan, and J. Tan. 2020. "Isogeometric Analysis of Functionally Graded CNT-Reinforced Composite Plates Based on Refined Plate Theory." *Journal of Mechanical Science and Technology* 34 (9): 3687– 3700. https://doi.org/10.1007/s12206-020-0821-0

[18] Maoudj, S., R. Tiberkak, M. E. Lazar, M. Ezzraimi, M. Bachene, and S. Rechak. 2023. "Free Vibration Analysis of Cracked Composite Plates Reinforced with CNTs Using Extended Finite Element Method (XFEM)." *Mechanics of Advanced Materials and Structures* 1–12. https://doi.org/10.1080/15376494.2023.2279703

[19] Mao, J., and W. Zhang. 2018. "Linear and Nonlinear Free and Forced Vibrations of Graphene Reinforced Piezoelectric Composite Plate under External Voltage Excitation." *Composite Structures* 203: 551–565. https://doi.org/10.1016/j.compstruct.2018.06.076

[20] Mehar, K., S. K. Panda, A. Dehengia, and V. R. Kar. 2015. "Vibration Analysis of Functionally Graded Carbon Nanotube Reinforced Composite Plate in Thermal Environment." *Journal of Sandwich Structures & Materials* 18 (2): 151–173. https://doi.org/10.1177/1099636215613324

[21] Quoc, T. H., T. M. Tu, and V. Van Tham. 2019. "Free Vibration Analysis of Smart Laminated Functionally Graded CNT Reinforced Composite Plates via New Four - Variable Refined Plate Theory." *Materials (Basel, Switzerland)* 12 (22): 1–22. https://doi.org/10.3390/ma12223675

[22] Reddy, J. N. 2004. *Mechanics of Laminated Composite Plates and Shells: Theory and Analysis* Boca Raton, FL: CRC Press.

[23] Rout, M., and S. S. Hota. 2023. "Geometrically Nonlinear Free Vibration of CNTs Reinforced Sandwich Conoidal Shell in Thermal Environment." *Acta Mechanica*234 (6): 2677–2694. https://doi.org/10.1007/s00707-023-03508-3

[24] Shams, S., and B. Soltani. 2015. "The Effects of Carbon Nanotube Waviness and Aspect Ratio on the Buckling Behavior of Functionally Graded Nanocomposite Plates Using a Meshfree Method." *Polymer Composites*. 38: 531–541. https://doi.org/10.1002/pc.23814

[25] Shen, H. 2009. "Nonlinear Bending of Functionally Graded Carbon Nanotube-Reinforced Composite Plates in Thermal Environments." Composite Structures 91 (1): 9–19. https://doi.org/10.1016/j.compstruct.2009.04.026

[26] Sobhy, Mohammed, and Fatemah H. H. Al Mukahal. 2023. "Magnetic Control of Vibrational Behavior of Smart FG Sandwich Plates with Honeycomb Core via a Quasi-3D Plate Theory." *Advanced Engineering Materials* 25 (13): 2300096. https://doi.org/10.1002/adem.202300096

[27] Uymaz, B., and G. Uymaz. 2023. "Three-Dimensional Thermal Vibration of CFFF Functionally Graded Carbon Nanotube-Reinforced Composite Plates." *Journal of Vibration Engineering & Technologies* 12 (4): 5345–5368. [Online]. Available https://doi.org/10.1007/s42417-023-00957-x

[28] Van Do, V. N., and C. Lee. 2022. "Nonlinear Bending Analysis of Carbon Nanotube-Reinforced Composite Plates in Combined Thermal and Mechanical." Acta Mechanica 233 (8): 3365–3391. https://doi.org/10.1007/s00707- 022-03268-6

[29] Wang, Z., and H. Shen. 2012. "Composites: Part B Nonlinear Vibration and Bending of Sandwich Plates with Nanotube-Reinforced Composite Face Sheets." *Composites Part B: Engineering* 43 (2): 411-421. https://doi.org/10.1016/j.compositesb.2011.04.040

[30] Wang, A., H. Chen, Y. Hao, and W. Zhang. 2018. "Vibration and Bending Behavior of Functionally Graded Nanocomposite Doubly-Curved Shallow Shells Reinforced by Graphene Nanoplatelets." *Results in Physics* 9: 550–559. https://doi.org/10.1016/j.rinp.2018.02.062

[31] Zaitoun, Mohamad W., Abdelbaki Chikh, Abdelouahed Tounsi, Alfarabi Sharif, Mohammed A. Al-Osta, Salah U. Al-Dulaijan, Mesfer M. Al-Zahrani, et al. 2023. "An Efficient Computational Model for Vibration Behavior of a Functionally Graded Sandwich Plate in a Hygrothermal Environment with Viscoelastic Foundation Effects." *Engineering with Computers* 39 (2): 1127–1141. https://doi.org/10.1007/s00366-021-01498-1

[32] Zhang, L. W., Z. G. Song, and K. M. Liew. 2015. "State-Space Levy Method for Vibration Analysis of FG-CNT Composite Plates Subjected to in-Plane Loads Based on Higher-Order Shear Deformation Theory." *Composite Structures* 134: 989-1003.https://doi.org/10.1016/j.compstruct.2015.08.138

[33] Zhu, R., E. Pan, and A. K. Roy. 2007. "Molecular Dynamics Study of the Stress –Strain Behavior of Carbon-Nanotube Reinforced Epon 862 Composites." *Materials Science and Engineering: A* 447 (1–2): 51–57. https://doi. org/10.1016/j.msea.2006.10.054

[34] Zhu, P., Lei, Z.X. and Liew K.M. 2012. "Static and free vibration analyses of carbon nanotube reinforced composite plates using finite element method with first order shear deformation plate theory." *Compos Struct*: 94 (4): 1450-1460. https://doi.org/10.1016/j.compstruct.2011.11.010